RSC Advances

ROYAL SOCIETY OF CHEMISTRY

PAPER

View Article Online
View Journal | View Issue

Check for updates

Cite this: *RSC Adv.*, 2025, **15**, 593

Direct observation of the interface reaction dynamics of the NdCeFeB phase *via in situ* annealing & quenching STEM†

Xiangyu Zhu,*[a] Qingxiao Wang,[ac] Li Shan,[d] Byung Oh Jung,[b] Myungshin Choi,[b] Sunyong Song,[b] Seok Namkung,[b] Namseok Kang,[b] Hui-Youn Shin,[b] Minho Joo,[b] Xianming Dai[d] and M. J. Kim*[a]

Received 20th May 2024
Accepted 18th December 2024

DOI: 10.1039/d4ra03708a

rsc.li/rsc-advances

Although the Rare Earth $(RE)_2Fe_{14}B$ type magnets were invented in the 1980s and are widely used worldwide. Yet, the phase formation and dissolution mechanisms are still not crystal clear. The reaction dynamics between rare earth elements (REE) and the iron-enriched matrix are essential to understanding the formation of hard magnetic REE–Fe–B phase or, conversely, phase dissociation and performance degeneration. Developing a reaction mechanism is fundamentally important for process engineering and performance manipulation. This work investigates the interface reaction dynamics between REE and an iron enriched matrix *via in situ* scanning transmission electron microscopy (STEM). The focused ion beam (FIB) procedure and *in situ* STEM experiments are specifically designed to achieve both oxygen-involved and oxygen-free reaction mechanisms within one specimen. The high-temperature reaction dynamics are frozen to room temperature (RT) by rapid quenching, preserving the solid–liquid interface dynamics between $Fe_{23}B_6$ and liquid phases. Serial atomic resolution STEM images depict lattice evolution while REE atoms embed into the $Fe_{23}B_6$ lattice. The presented work also demonstrates that combining an advanced FIB procedure with *in situ* annealing & quenching STEM is a powerful tool for investigating the complex system's high-temperature reaction mechanisms and interface phenomena.

1. Introduction

The ever-increasing market demand for REE–Fe–B type hard magnetic material in auto, energy, and electric device fields raises up-and-coming challenges on material engineering at cost and performance optimization.[1–3] In particular, Ce-substituted NdFeB magnets have attracted broad research interest in both industrial and academic prospects owing to decent magnetic properties (coercivity, energy density) and unique cost *vs.* performance ratio.[4–7] However, current studies are mainly focused on phase identification, microstructural features, and macroscopic magnetic properties with less insight at the nanoscale and reaction mechanism, which is also fundamental to explaining phase transformation and morphology evolution mechanisms. Even though the reaction of the Ce–Nd–Fe–B quaternary system is complex (even more complex if considering oxygen[8,9]), a study on the thermally induced evolution dynamics is a principal that facilitates the manufacturing of high-quality magnets.[10,11] In particular, the reaction behavior between REE and the iron enriched matrix is still unclear, which may hinder thermal treatment design and microstructure optimization. Metastable iron boride phases ($Fe_{23}B_6$ and Fe_3B) are considered the precursors that generate a RE–Fe–B type hard magnetic phase *via* dissolving the REE atoms within the lattice. Several hypotheses have been proposed accordingly.[12–14] Still, direct experimental evidence is missing so far.

Direct observation of the crystal interface reaction during growth is of paramount significance to establish the understanding of boundary phase-change kinetics and further govern the magnetic performance, material reliability, and dissociation behavior of magnet materials. To this end, *in situ* STEM is the desired characterization technique combing the external stimuli (thermal, electrical, and atmosphere) with atomic resolution imaging capability in real time. Our recent *in situ* annealing STEM study pushed the insights on elemental diffusion and phase evolution behavior of $(Nd_{0.75}Ce_{0.25})_2Fe_{14}B$ material down to the sub-nanometer scale.[15] The result shows the REE tends to react with oxygen starting from 200 °C and

---

[a] *Department of Materials Science and Engineering, University of Texas Dallas, 800 W Campbell Rd, Richardson, TX, 75080, USA. E-mail: moonkim@utdallas.edu; X.Y_Zhu@outlook.com*

[b] *Materials & Devices Advanced Research Institute, LG Electronics, LG Science Park, 10, Magokjungang 10-ro, Gangseo-gu, Seoul, 07796, Korea*

[c] *Imaging and Characterization Core Lab, King Abdullah University of Science and Technology (KAUST), Thuwal, 23955-6900, Saudi Arabia*

[d] *Department of Mechanical Engineering, University of Texas at Dallas, 800 W Campbell Rd, Richardson, TX, 75080, USA*

† Electronic supplementary information (ESI) available. See DOI: https://doi.org/10.1039/d4ra03708a

diffuse into the grain boundary area. It has been widely demonstrated that the REE-enriched grain boundary phase is essential for performance optimization. It acts as a domain boundary and enhances the coercivity by lowering the short-range exchange coupling between adjacent grains.[16–18] At the same time, the reaction between the REE-enriched phase and the iron boride phase is considered the initial reaction that forms the Ce–Nd–Fe–B phase and generates the hard magnetic properties.[12–14] Yet, the oxygen-involved phase dissociation at high-temperature behavior seems avoidable or reversible in the real world or under *in situ* STEM experiment conditions. The REE atoms are mostly oxygen-deprived and transformed to the oxide phase under thermal stimuli. Thus, unfortunately, the dissolving process of the NdCe enriched phase into the iron boride phase remains a black box to researchers, which is critical for the crystallization of the NdCeFeB hard magnet phase.

This research aims to directly observe the dissolving process of REE atoms into an iron boride matrix *via* in-site annealing and quenching STEM experiment. A two-step FIB sample preparation procedure is specially designed to achieve the observation of oxidized and oxygen-free areas in sequence. First, annealing at 700 °C produces the metastable stable phase $Fe_{23}B_6$ and NdCe enriched liquid phase system, then rapid quenching interrupts the reaction in between and fixes the interface dynamics. In particular, the lattice structure of the solid–liquid interface and short-range order are analyzed at an atomic scale. Our results reveal the crystallization interface morphology of the REE atoms embedded into the $Fe_{23}B_6$ phase and shade lights on the formation mechanism of NdCeFeB magnet phases.

2. Experiment

2.1 Synthesis of NdCeFeB alloy

The $RE_2Fe_{14}B$ type (tetragonal, $P4_2/mnm$) with nominal compositions of $(Nd_{0.75}Ce_{0.25})_{12.9}Fe_{76.47}Co_{4.5}Ga_{0.53}B_{5.6}$ (at%) polycrystalline samples were used in this study.[15] Alloy ingots were made by induction melting furnace with nominal constituent composition under an argon atmosphere. The as-cast ingots were melt-spun onto a molybdenum wheel from a calcium oxide (CaO) crucible with a surface speed of about 30 m s^{-1} to obtain nanocrystalline ribbons. The physical dimensions of synthesized ribbons are 1.5 mm in width, 5 mm in length, and 0.1 mm in thickness. These ribbons exhibit uniform and smooth surface morphology, as confirmed by SEM image (Fig. 1a and b), with defects-free surfaces benefiting from the rapid cooling process. The rapid solidification results in a nanocrystalline structure with grain sizes typically tens of nanometers. This fine microstructure promotes the magnetic properties of the ribbons particularly through enhanced coercivity and energy density.

2.2 FIB sample preparation

The FIB technique was used to create a cross-sectional lamella from the bulk melt-spun ribbon. First, 2 μm protection deposition (carbon and Pt layer) is reacted on the material surface to avoid ion-beam damage. Then, two rough millings are performed to create a deep hole and isolate the target area. A U-cut milling approach was employed, followed by a lift-out using a nanoprobe to transfer the lamella onto an *in situ* heating chip. The region 2 of lamella was then thinned to a thickness of approximately 100 nm to ensure electron transparency for STEM analysis. The 3D modeling of the FIB sample for *in situ* annealing is shown in ESI S1.†

To achieve regions with distinct oxygen concentrations, the sample was strategically prepared using the following steps Fig. 1(c–g):

- Region 1 (oxygen-free): this region was left un-thinned (∼3 μm thickness) before annealing, ensuring it remained encapsulated by the surrounding bulk material and isolated from ambient oxygen during transfer and annealing. After annealing, another FIB cut is performed on the un-thinned region 1 area and lifted out.
- Region 2 (oxygen-exposed): this region was thinned to 100 nm before annealing, exposing it to trace levels of surface-absorbed oxygen during transfer and the *in situ* annealing process.

2.3 *In situ* STEM annealing and quenching experiment

The *in situ* microelectromechanical system is based on Protochips Aduro TEM holder and heating E-chips. *In situ* STEM samples were prepared by a focus ion beam (FEI Nova 200) instrument equipped with a nanoprobe (Omniprobe 200) for lift-out operation. The structural and elemental analysis was done by cs-corrected scanning transmission electron microscope (JEOL ARM 200F) operated at 200 kV equipped with Energy Dispersive X-ray Spectroscopy (EDS) (Oxford X-MaxN100TLE with 100 mm^2 silicon drift detector). The acquisition semi-angle for high angle annular dark field (HAADF) detector and annular bright field (ABF) detector was 90–370 mrad and 12–24 mrad, respectively.

3. Results

The *in situ* experiment and two-step FIB procedure are specifically designed, aiming to eliminate the oxidation effect before observation (Fig. 1). The oxygen concentration is closely related to the thermally induced evolution behavior of REE, which could lead to the formation of Nd–Ce–Fe–B phase with oxygen-free surrounding, or conversely phase dissociation and hard magnetic properties degeneration caused by the loss of main phase. Here we describe the experiment in three parts: (I) sample preparation for the *in situ* experiment using FIB; (II) *in situ* annealing and quenching STEM experiment; (III) second FIB sample preparation and STEM observation after the *in situ* experiment. The crystal–liquid interface is observed in region 1 after quenching, which is oxygen free whereas region 2 is set as a control group because the reaction is affected by oxygen (Fig. 1).

(I) Fig. 1a–c illustrates the sample preparation and transfer operation *via* FIB. A melt-spun $(Nd_{0.75}Ce_{0.25})_2Fe_{14}B$ ribbon is

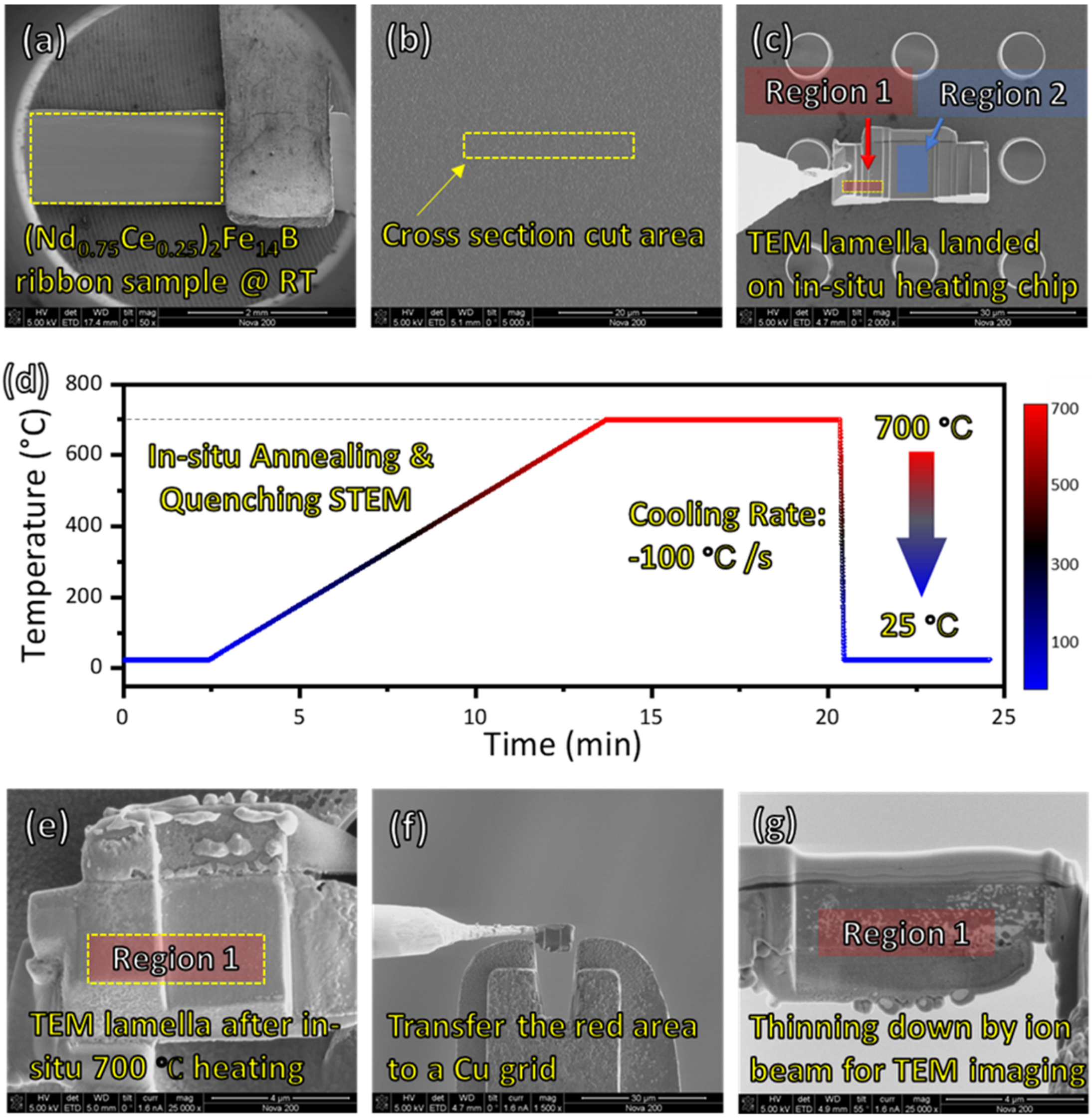

Fig. 1 Sample preparation under SEM/FIB view (a) $(Nd_{0.75}Ce_{0.25})_2Fe_{14}B$ ribbon sample is fixed by a Cu tip on the stage; (b) sample surface shows uniform morphology; (c) TEM lamella placed on an *in situ* heating chip; (d) *in situ* rapid quench temperature *vs.* time diagram; (e) sample after the *in situ* quench experiment; (f) FIB milling and transfer the quenched sample on Cu grid; (g) thinning specimen down to ~100 nm for STEM analysis.

fixed on a stage by a Cu tip (Fig. 1a), and even contrast indicates the uniformity of the sample. The cross-section cut area is selected randomly as indicated by Fig. 1b yellow marker ($15 \times 2\ \mu m^2$). After ion-beam milling and U-cut, the sample is transferred on an *in situ* heating E-chip (Fig. 1c). Here, two areas are selected for STEM observation with different reaction mechanisms due to oxygen concentration differences. Region 1, marked by red color, is not thinned (~3 μm) before annealing. Thus the area is covered by the material and isolated to oxygen before annealing. By comparison, region 2 is thinned down to 100 nm before annealing and is exposed to the atmosphere during the transfer process from FIB to the STEM chamber. Although the *in situ* annealing is operated under pressure as low as 10^{-6} torr, the tiny amount of surface-absorbed oxygen does affect the reaction mechanism of region 2.

(II) The temperature *vs.* time diagram of the *in situ* annealing & quenching experiment is indicated by Fig. 1d. Strat from room temperature 25 °C, the sample is heated up to 700 °C for 7 min with a 1 °C s^{-1} ramping rate. Then the sample was quenched down to 25 °C with a 100 °C s^{-1} cooling rate that frozen the reaction inside. The detailed temperature recording and thermal condition of the *in situ* sample are discussed in the ESI (S2†). At stage II, the STEM imaging and EDS mapping are focused on region 2 (*i.e.*, oxygen-involved reaction).

(III) After the *in situ* quenching experiment, a cross-section FIB cut was made to the left thick region of the quenched sample (Fig. 1e) and transferred on a Cu grid (Fig. 1f). Then, the sample was thinned down to 100 nm for STEM observation (Fig. 1g). At stage III, the STEM imaging and elemental mapping are focused on region 1 (*i.e.*, the oxygen-free reaction region).

The morphology and elemental distribution at regions 1 and 2 are shown in Fig. 2a–e and f–l respectively. Before *in situ* annealing, the $(Nd_{0.75}Ce_{0.25})_2Fe_{14}B$ sample exhibits uniform morphology (Fig. 2f). EDS line scan (Fig. 2g) shows a gradient decreasing oxygen concentration from the top surface to inside, and the concentration of Fe, Nd, and Ce increase accordingly with a specific ratio. The EDS line scan result confirms the existence of absorption oxygen at the bulk surface. The atomic concentration of oxygen is significantly high near the surface (0–500 nm) compared with the area inside the sample (ESI S3†). (Accordingly, the second FIB cut at region 1 is selected at around 5 μm depth under the surface to minimize oxygen absorption.) The observed trend arises from the preparation method—melt spun. The molten alloy is rapidly cooled during melt spinning as it contacts a rotating chilled substrate. The rapid cooling rate limits the diffusion of oxygen into the bulk but allows oxygen to interact with the exposed surface. As a result, the surface of ribbons is enriched with oxygen element.[19,20] After annealing and quenching, the phase decomposition reaction is found in both regions. The Fe-enriched phase is separated from the Nd & Ce enriched phase at region 1 (Fig. 2b–d) and region 2 (Fig. 2i–k). The characteristic X-ray oxygen signal (Fig. 2l) of region 2 overlaps with Nd and Ce signals, indicating the formation of the rare earth oxide phase. By comparison, the oxygen signal (Fig. 2e) of region 1 is uniformly distributed, meaning oxygen is not involved in the reaction. We believe oxygen concentration is the major factor determining the different reaction mechanisms between region 1 and region 2. The presented work mainly focuses on the phase evolution and interface dynamics in region 1, which is an

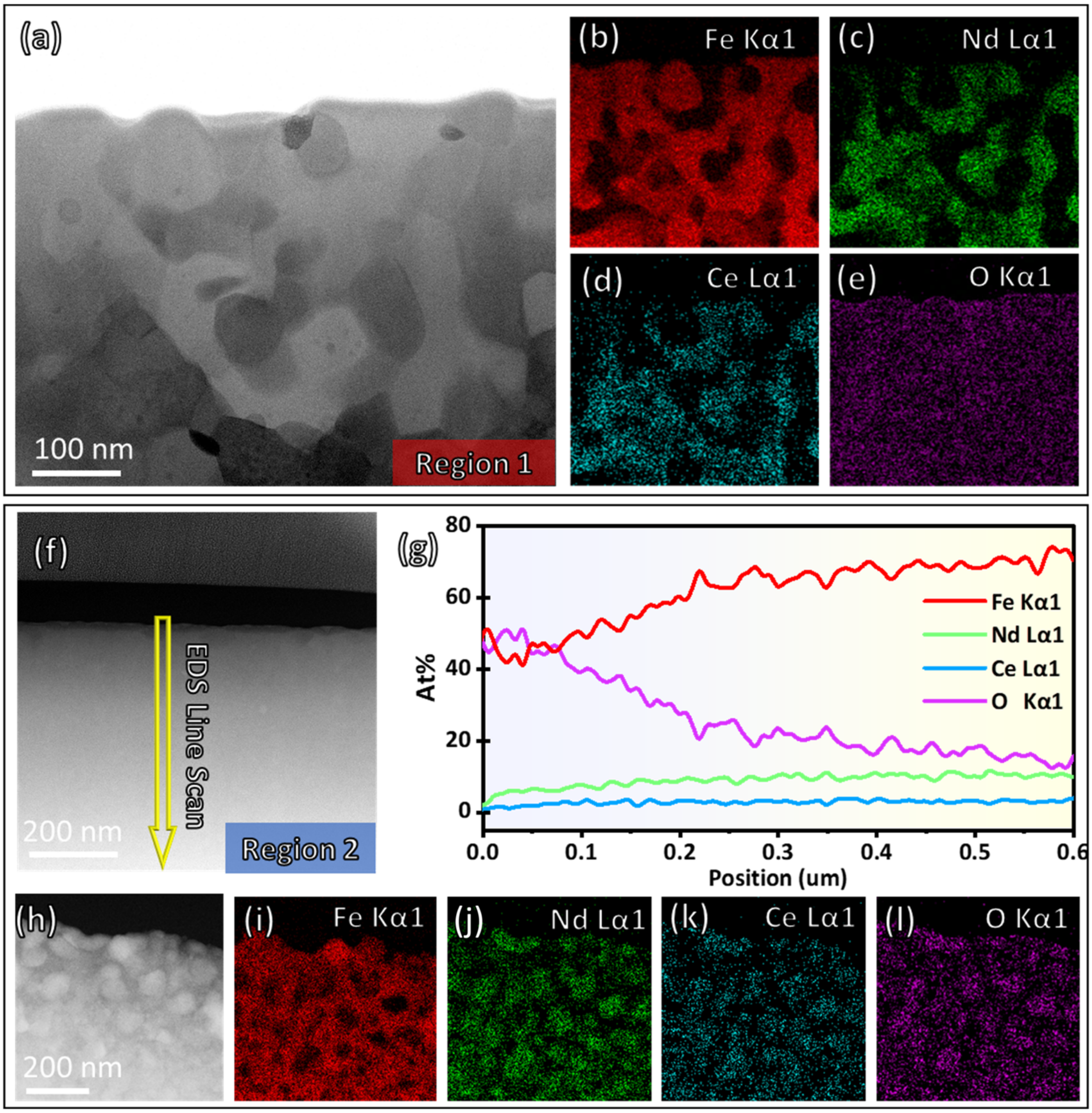

Fig. 2 Morphology and elemental distribution of $(Nd_{0.75}Ce_{0.25})_2Fe_{14}B$ after annealing (a) STEM-ABF image showing region 1 morphology after 700 °C annealing; (b–e) EDS mapping of Fe, Nd, Ce, and O elements in region 1 respectively; (f) STEM-HAADF image showing a cross-section view of $(Nd_{0.75}Ce_{0.25})_2Fe_{14}B$ ribbon at region 2 before annealing; (g) EDS line scan at (f) area showing the concentration of O element; (h) STEM-HAADF image of region 2 after 700 °C annealing; (i–l) EDS mapping of Fe, Nd, Ce, and O elements of the region (h), respectively.

oxygen-free reaction. The detailed sample structure at room temperature and oxygen-involved reaction dynamics of the Nd–Ce–Fe–B system were introduced in our recent publication with a similar experiment setup and phenomenon observed in region 2.[15]

Three phases are found in region 1 after *in situ* annealing & quenching, α-Fe, $Fe_{23}B_6$, and REE-enriched amorphous phases. The typical crystal–liquid interface between $Fe_{23}B_6$ and REE-enriched amorphous phases is shown in Fig. 3a. The top area is a metastable phase $Fe_{23}B_6$ lattice, and the bottom area is an amorphous phase considered a liquid phase at high temperature. EDS (Fig. 3b–d) and EELS (Fig. 3e) mappings show the Fe and B elements constitute the metastable phase $Fe_{23}B_6$, and rare earth elements are enriched in the liquid phase. Still, the oxygen signal (Fig. 3f) is uniformly distributed among the interface at the nanoscale, proving that oxygen was not involved in the reaction of region 1. The intensity gradient of Fe, Nd, Ce, and B elemental mapping at the phase interface exhibits a moderate variation, indicating the tendency of elemental interdiffusion behavior. The metastable phase $Fe_{23}B_6$ is crystallized as a face-centered cubic (FCC) lattice structure, *Fm3m* space group.[21,22] This soft magnetic phase has high saturation magnetization ($\mu_0 M_S = 1.7$ T) and a relatively low anisotropy constant (0.01 MJ m^{-3}).[12] The lattice structure of $Fe_{23}B_6$ crystal along [001], [111], and [112] are shown in Fig. 3g–i, respectively. The lattice map is generated by Vesta software[23] based on a crystal CIF file obtained from standard database[24] and overlaid on STEM image manually. The supercell ($Fe_{92}B_{24}$) of the $Fe_{23}B_6$ crystal, including four unit cells ($Fe_{23}B_6$), is presented in atomic resolution STEM images that illustrate the full symmetry elements of the lattice. Namely, as defined by Wyckoff notation, there are four inequivalent iron sites, 4a, 8c, 32f, and 48h, and 24 boron sites at 24e within the $Fe_{92}B_{24}$ supercell.[25] The lattice constant could be represented as $a = b = c = 10.6$ Å, $\alpha = \beta = \gamma = 90°$. Notably, the metastable $Fe_{23}B_6$ phase is considered as the precursor of $RE_2Fe_{14}B$ type magnet during the crystallization sequence,[12] and so the interface reaction with the REE-enriched phase is worth investigating in detail to explore the early phase formation mechanism.

The interface dynamics between the REE-enriched phase and the $Fe_{23}B_6$ metastable phase are analyzed at the sub-nano scale through STEM images and EELS/intensity profiles acquired simultaneously. Fig. 4 exhibits three types of crystal–liquid interface structure and the corresponding elemental distribution analysis that reveals the REE embedded into the $Fe_{23}B_6$ lattice.

(I) The interface structure between $Fe_{23}B_6$ and the liquid phase is illustrated in Fig. 4a, which could be considered as the

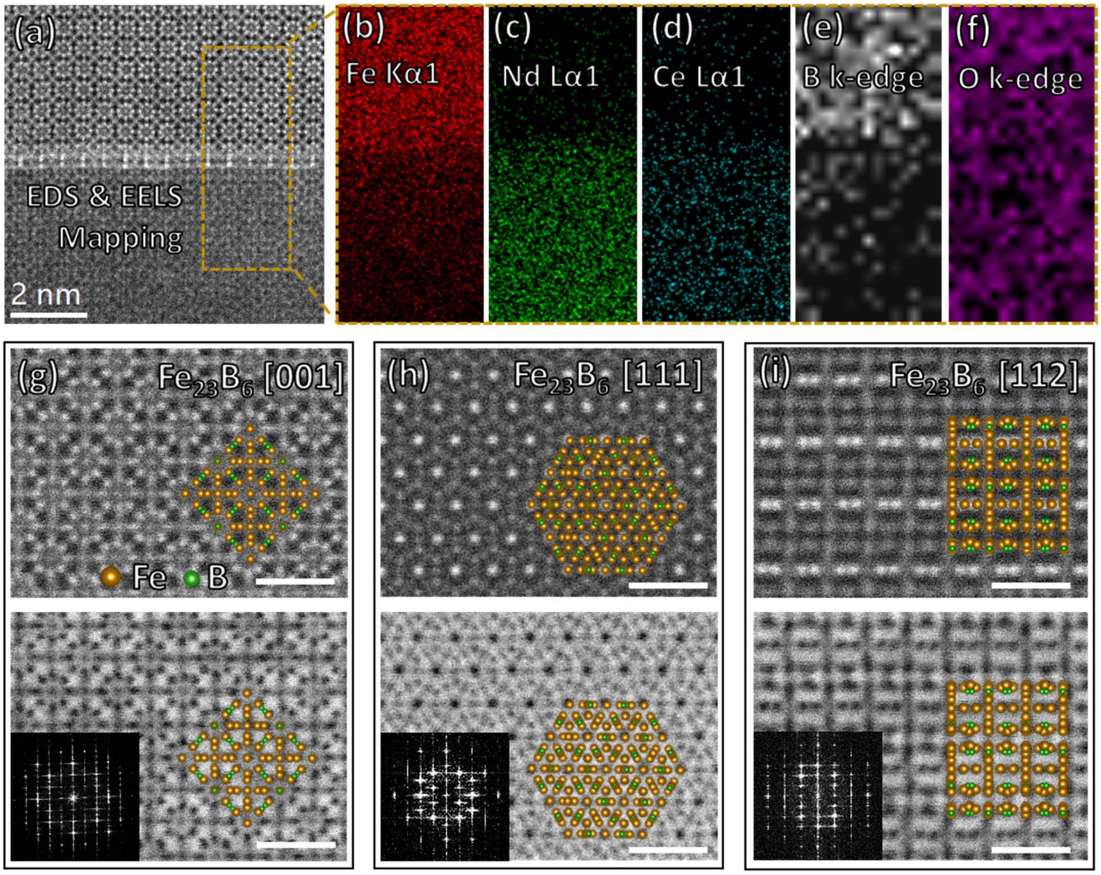

Fig. 3 Elemental distribution at the interface and $Fe_{23}B_6$ structure analysis (a) STEM-HAADF image showing a typical interface structure between $Fe_{23}B_6$ and liquid phase; (b–d) EDS mapping of Fe, Nd, and Ce elements, respectively; (e and f) EELS mapping of B and O elements, respectively; (g–i) STEM-HAADF and STEM-ABF images showing $Fe_{23}B_6$ crystal structure along [001], [111], and [112] zone axis, scale bar is 1 nm.

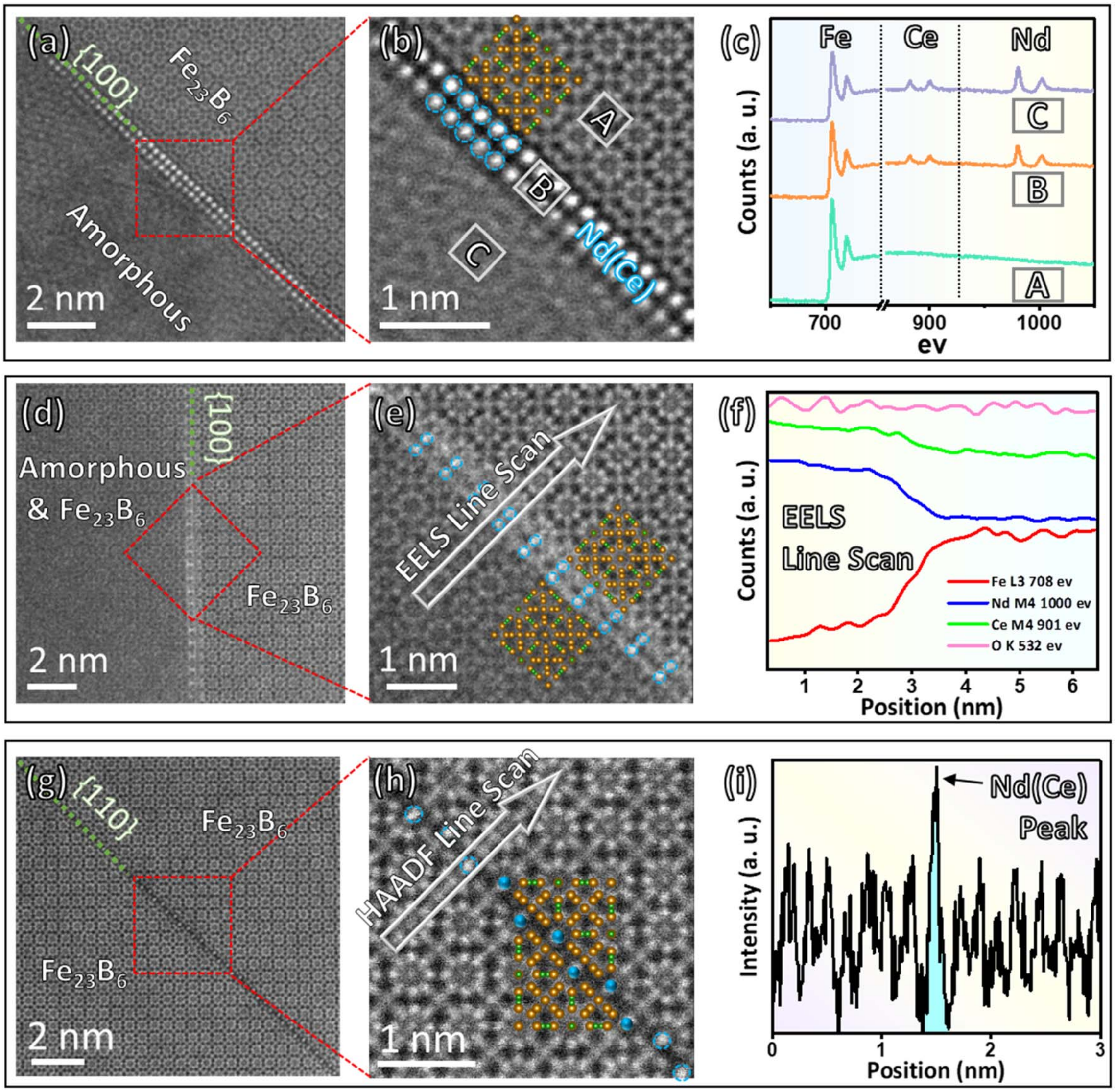

Fig. 4 $Fe_{23}B_6$–NdCe interface structure analysis (a and b) STEM-HAADF image showing $Fe_{23}B_6$ and liquid phase interface structure; (c) EELS spectrum collected at $Fe_{23}B_6$ area, interphase film, and liquid phase, respectively; (d and e) STEM-HAADF image showing $Fe_{23}B_6$ and (liquid + $Fe_{23}B_6$) interface structure with NdCe enriched boundary; (f) EELS line scan across the $Fe_{23}B_6$ and (liquid + $Fe_{23}B_6$) interface; (g and h) STEM-HAADF image showing defect structure of $Fe_{23}B_6$ with NdCe substitutional atoms; (i) intensity profile of STEM-HAADF images identifies the NdCe substitutional atoms at 4a site.

initial reaction state between rare earth elements and the $Fe_{23}B_6$ phase. The amorphous shown in the lower-left corner is a liquid phase formed after 700 °C annealing, and the atomic ratio of the amorphous area is about Nd (3) : Ce (1) : Fe (1), verified by EDS. The upper-right corner is $Fe_{23}B_6$ lattice with ⟨001⟩ zone axis, and the coherent edge is along {100} plane. The high-magnification HAADF image (Fig. 4b) shows the interface structure at an atomic scale. The two-atom-thick interphase layer is marked by a blue circle that separates the $Fe_{23}B_6$ lattice and liquid phase on two sides. The atomic configuration of the interphase layer along the edge is incorporated with the {004} plane of the $Fe_{23}B_6$ lattice, exhibiting good crystallographic coherency at the interface in between. EELS spectrum (Fig. 4c) provides qualitative element analysis at $Fe_{23}B_6$ area 'A', the interphase film 'B', and the liquid phase 'C'. Compared with "A" site, the interface "B" site is enriched with Nd and Ce, which is very similar to the liquid phase. By comparison, the intensity of Nd and Ce characteristic peaks is negligible at the 'A' site, indicating a minimum Nd and Ce concentration in the $Fe_{23}B_6$ lattice.

(II) The $Fe_{23}B_6$ and (liquid + $Fe_{23}B_6$) interface structure is featured in Fig. 4d. At this state, the $Fe_{23}B_6$ lattice grows toward the liquid phase side, and the Nd and Ce atom start to embed into the $Fe_{23}B_6$ lattice. The (liquid + $Fe_{23}B_6$) phase on the lower-left side is the combination of the $Fe_{23}B_6$ phase and rare earth elements enriched liquid phase, as the lattice fringe is nearly visible with relatively poor contrast compared with the pure $Fe_{23}B_6$ phase area on the upper-right side. Fig. 4e exhibits the interface structure at an atomic scale. Still, a rare earth element enriched two-atom-thick film could be identified by brightness difference at the interface, as the intensity in HAADF-STEM images is approximatively proportional to Z^2 (Z is the atomic number).[26] The intergranular films crystallize coherently with {002} plane of the $Fe_{23}B_6$ lattice marked by a blue circle. Yet, the atomic configuration of the interface area could not be fully distinguished as the crystallization process has not finished, shown as bright stripes and random dots in the region of the intergranular films. The elemental distribution of $Fe_{23}B_6$ and (liquid + $Fe_{23}B_6$) interface structure is analyzed by EELS line scan (Fig. 4f). Similar to the previous result, the rare earth elements (Nd and Ce) are enriched at the liquid phase and interface area. The Fe intensity exhibits a gradient drop from the pure $Fe_{23}B_6$ lattice side to the (liquid + $Fe_{23}B_6$) phase side, indicating the directional diffusion behavior, so the crystal growth direction is predictable on the liquid side.

(III) At the crystallized area, the rare earth element atoms from the liquid phase dissolve inside the $Fe_{23}B_6$ lattice. Fig. 4g demonstrates a substitutional defect structure of $Fe_{23}B_6$ lattice along the {110} plane with the one-atom-thick layer. The 4a site atoms are marked by a blue circle (Fig. 4h), and the intensity line scan profile (Fig. 4i) shows the brightness of marked atoms is significantly higher than other sites Fe atoms inside the $Fe_{23}B_6$ lattice. The exceptional brightness peak observed by the STEM-HAADF image indicates the selective metallic site occupation behavior of Nd and Ce atoms in the $Fe_{23}B_6$ lattice. The similar selective substitutional behavior in $Fe_{23}B_6$ type crystal was predicted *via* the atomistic simulation method and proved 4a site is the most energy-favorable atomic replacement site preference.[27]

4. Discussion

This work describes two types of phase transformation mechanisms of $(RE)_2Fe_{14}B$ phase (Fig. 5a). Oxygen concentration is

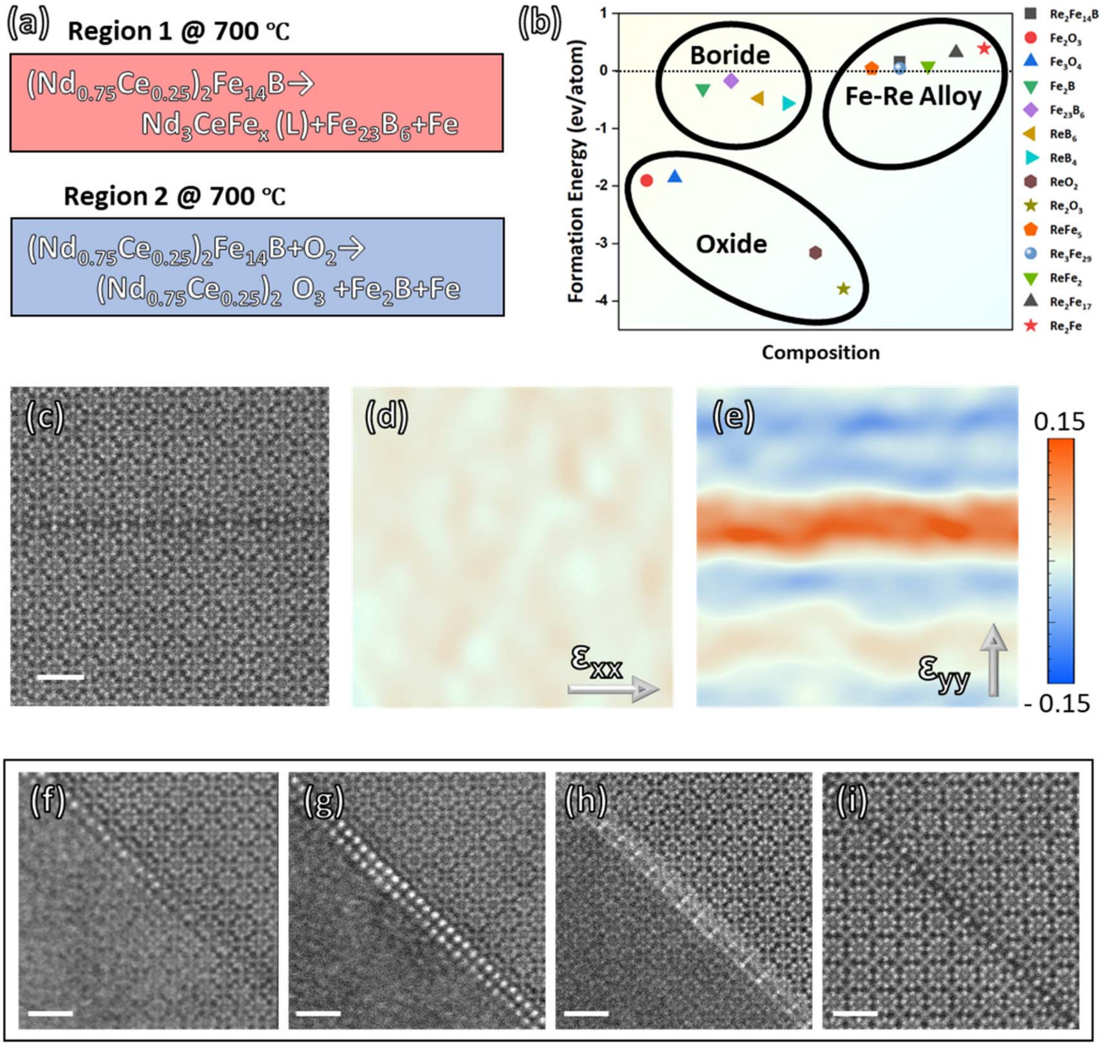

Fig. 5 Reaction mechanism of Nd–Ce–Fe–B system (a) unbalanced phase transformation equation with oxygen (blue) and without oxygen (red); (b) the formation energy of phases with Nd–Ce–Fe–B–O system (Rare Earth (RE) used in the figure represent $Nd_{0.75}Ce_{0.25}$); (c–e) geometrical phase analysis (GPA) of the substitutional area in $Fe_{23}B_6$ lattice, the number in color bar represents the quantitative values of strain; (f–i) $Fe_{23}B_6$ & liquid phase interface evolution dynamics. The scale bar is 1 nm.

the major factor governing the reaction mechanism at 700 °C of $(Nd_{0.75}Ce_{0.25})_2Fe_{14}B$ material. *In situ* STEM experiment investigates the thermally induced phase evolution behavior in regions 1 (oxygen-free) and 2 (oxygen-involved) with the same heat condition but different oxygen concentrations. In region 1, the main phase decomposes as $Fe_{23}B_6$, α-Fe, and REE enriched liquid phases. In contrast, region 2 generates Fe_2B, α-Fe, and REE oxide phases that are more thermodynamically favorable compared with phases in region 1 (Fig. 5b). Especially, the formation energy of oxide phases is significantly lower compared with boride phases and Fe–Re alloy phases in the system.[24] Thus, oxygen tends to deprive the REE elements in the Nd–Ce–Fe–B system and form the REE oxide phase, which hinders the regeneration of the hard magnetic phase. The REE deprivation discussed in this work also explains the thermally induced irreversible degeneration of hard magnetic properties. By comparison, in the oxygen-free system, the REE enriches into the liquid phase and seems to stabilize the metastable phase $Fe_{23}B_6$, which is considered the precursor of the $Re_2Fe_{14}B$ type phase. Therefore, the interface evolution between $Fe_{23}B_6$ and the liquid phase is worth exploring to understand the reaction dynamics.

The structure of metastable phase $Fe_{23}B_6$ allows partial occupation of metal sites and lattice constant variations that optimize magnetic moment.[28–30] Also, the substitution REE atoms introduce a significant lattice distortion into the lattice along the [110] direction inside the matrix lattice (Fig. 5c–e) and enhance the crystal magnetic anisotropy according to Neumann's principle.[31–33] Previous studies indicate that dissolving REE atoms is the critical step that transfers the iron boride matrix from ‘soft’ to ‘hard’ magnetic properties.[12–14] The dissolving behavior of REE into the $Fe_{23}B_6$ matrix is investigated directly *via in situ* annealing & quenching STEM experiments for the first time in this work. After annealing and main phase dissociation at 700 °C, the $Fe_{23}B_6$ & liquid phase crystal–liquid interface (Fig. 5f) is fixed during the reaction process *via* rapid quenching with a 100 °C s^{-1} cooling rate. As a result, Nd and Ce atoms are found to separate from the liquid phase and crystallize at the surface of the $Fe_{23}B_6$ phase (Fig. 5g). The atomic configuration of the interphase layer is coherent with the $Fe_{23}B_6$ lattice. Likewise, Fe atoms are found to diffuse across the interphase layer and form an iron boride phase at the liquid phase side, and as a result, Nd and Ce atoms embed inside the $Fe_{23}B_6$ lattice (Fig. 5h–i). Although the morphology observed is ‘static’ at room temperature, the unbalanced solidification process creates various interface morphology that provides insights into the early nucleation dynamics of the Nd–Ce–Fe–B phase.

5. Summary

The present work extensively used advanced FIB-STEM and elemental analysis techniques to study the thermally induced phase evolution and crystal–liquid interface structure of the Nd–Ce–Fe–B system with unprecedented detail. The sample preparation and *in situ* experiment procedure are specifically designed to achieve both oxygen-involved and oxygen-free reaction mechanisms within one FIB-prepared specimen. $(Nd_{0.75}Ce_{0.25})_2Fe_{14}B$ sample is annealed at 700 °C for 7 min and then quenched to 25 °C with a 100 °C s^{-1} cooling rate that ‘frozen’ the crystal–liquid interface for observation. The angstrom scale atomic structural analysis and sub-nanometer spatial resolution elemental analysis clearly revealed the lattice evolution and element diffusion behavior between metastable $Fe_{23}B_6$ solid phase and REE enriched liquid phase. This combination of advanced FIB and *in situ* STEM techniques was proved as a powerful method to reveal the phase evolution mechanisms and reaction dynamics of complex composition systems. The following summaries briefly introduce the results presented above.

(I) Oxygen concentration is the major factor determining the phase evolution mechanism of $(Nd_{0.75}Ce_{0.25})_2Fe_{14}B$ magnet, depriving REE atoms of matrix forming oxide phase. Therefore, the unbalanced phase transformation equations at 700 °C could be represented as:

- $(Nd_{0.75}Ce_{0.25})_2Fe_{14}B \rightarrow Nd_3CeFe_x\ (L) + Fe_{23}B_6 + \alpha\text{-Fe}$
- $(Nd_{0.75}Ce_{0.25})_2Fe_{14}B + O_2 \rightarrow (Nd_{0.75}Ce_{0.25})_2O_3 + Fe_2B + \alpha\text{-Fe}$

(II) The REE atoms from the liquid phase are found to crystallize at the surface of the $Fe_{23}B_6$ lattice, forming an atomic coherent interphase layer. Fe elements diffused toward the liquid phase side that facilitates the $Fe_{23}B_6$ crystal growth across the REE-enriched interface layer. As a result, Nd and Ce atoms become substitutional atoms and are embedded in the $Fe_{23}B_6$ lattice, forming the Nd–Ce–Fe–B phase.

This study demonstrates that oxygen concentration is a dominant factor influencing Nd–Ce–Fe–B alloys' reaction dynamics and phase evolution. Specifically, the substitution of Nd and Ce into the $Fe_{23}B_6$ lattice was directly observed for the first time, providing atomic-scale evidence of the mechanisms underlying hard magnetic phase formation. These findings not only enhance our fundamental understanding of the Nd–Ce–Fe–B system but also offer guidance to the optimization of thermal treatment protocols and oxygen control strategies to enhance the performance and longevity of REE–Fe–B magnets, with potential benefits for automotive, energy, and electronic device applications. Additionally, this research highlights the extraordinary capabilities of combining advanced FIB and *in situ* STEM technologies to investigate high-temperature reaction dynamics at unprecedented spatial resolution.

Data availability

The data supporting this study's findings are available from the corresponding author upon reasonable request.

Author contributions

Xiangyu Zhu wrote the manuscript and carried out the FIB and STEM experiment with Qingxiao Wang. Li Shan and Xianming Dai provided finite element analysis. Byung Oh Jung, Myungshin Choi, Sunyong Song, Seok Namkung, Namseok Kang, Hui-Youn Shin, and Minho Joo synthesize the material. M. J. Kim and Xiangyu Zhu supervised and conceived this project.

Conflicts of interest

The authors declare that they have no known competing financial interests or personal relationships that could have appeared to influence the work reported in this paper.

Acknowledgements

This research was supported by the Materials & Devices Advanced Research Institute (MDARI), one of the research centers at LG Electronics. The authors are grateful for the assistance of Dr Jeong Soo Lee (Head of MDARI). The UTD research was supported in part by the Louis Beecherl, Jr Endowed funds. Finally, the author acknowledges Yaoqiao Hu for providing suggestions for thermodynamics analysis.

References

1 M. V. Reimer, H. Y. Schenk-Mathes, M. F. Hoffmann and T. Elwert, *Metals*, 2018, **8**, 867.
2 C. Li, J. M. Mogollón, A. Tukker, J. Dong, D. von Terzi, C. Zhang and B. Steubing, *Renewable Sustainable Energy Rev.*, 2022, **164**, 112603.
3 J. M. D. Coey, *Engineering*, 2020, **6**, 119–131.
4 M. Zhang, W. Zhang, F. Chen, Y. Guo, F. Li and W. Liu, *J. Supercond. Novel Magn.*, 2018, **31**, 2811–2816.
5 T. Miyake, Y. Harashima, T. Fukazawa and H. Akai, *Sci. Technol. Adv. Mater.*, 2021, **22**, 543–556.
6 G. Y. Kim, T. H. Kim, H. R. Cha, S. hyub Lee, D. H. Kim, Y. Do Kim and J. G. Lee, *J. Mater. Sci. Nanotechnol.*, 2022, **126**, 71–79.
7 G. Y. Kim, T. H. Kim, H. R. Cha, S. hyub Lee, D. H. Kim, Y. Do Kim and J. G. Lee, *Scr. Mater.*, 2022, **214**, 114676.
8 D. C. Nababan, R. Mukhlis, Y. Durandet, M. I. Pownceby, L. Prentice and M. A. Rhamdhani, *Corros. Sci.*, 2021, **182**, 109290.
9 D. C. Nababan, R. Mukhlis, Y. Durandet, M. I. Pownceby, L. Prentice and M. A. Rhamdhani, *Corros. Sci.*, 2021, **189**, 109560.
10 T. Abe, M. Morishita, Y. Chen, A. Saengdeejing, K. Hashimoto, Y. Kobayashi, I. Ohnuma, T. Koyama and S. Hirosawa, *Sci. Technol. Adv. Mater.*, 2021, **22**, 557–570.
11 S. Kobayashi, T. Abe, A. Martín-Cid, S. Kawaguchi, M. Suzuki, S. Hirosawa and T. Nakamura, *J. Alloys Compd.*, 2022, **892**, 162188.
12 O. Gutfleisch, *J. Phys. D Appl. Phys.*, 2000, **33**(17), R157.
13 E. Kneller and R. Hawig, *IEEE Trans. Magn.*, 1991, **27**, 3588–3560.
14 Y. C. Jung and K. Nakai, *Met. Mater. Int.*, 2003, **9**, 337–344.
15 X. Zhu, B. Oh Jung, Q. Wang, Y. Hu, M. Choi, S. Song, S. Namkung, N. Kang, H. Y. Shin, M. Joo and M. J. Kim, *Mater. Des.*, 2022, **216**, 110525.
16 Z. Liu, J. He and R. V. Ramanujan, *Mater. Des.*, 2021, **209**, 110004.
17 L. Zhao, J. He, W. Li, X. Liu, J. Zhang, L. Wen, Z. Zhang, J. Hu, J. Zhang, X. Liao, K. Xu, W. Fan, W. Song, H. Yu, X. Zhong, Z. Liu, X. Zhang, L. Zhao, X. Liu, J. Zhang, L. Wen, Z. Zhang, X. Zhang, J. He, J. Hu, X. Liao, K. Xu, W. Fan, W. Song, H. Yu, X. Zhong, Z. Liu and W. Li, *Adv. Funct. Mater.*, 2022, **32**, 2109529.
18 J. Ni, T. Ma and M. Yan, *J. Magn. Magn. Mater.*, 2011, **323**, 2549–2553.
19 H. Zheng, W. Wang, J. Yu, Q. Zhai and Z. Luo, *J. Mater. Res.*, 2014, **29**, 880–886.
20 D. J. Sordelet, X. Y. Yang, E. A. Rozhkova, M. F. Besser and M. J. Kramer, *Appl. Phys. Lett.*, 2003, **83**, 69–71.
21 V. A. Barinov and V. T. Surikov, *Phys. Met. Metallogr.*, 2008, **105**(3), 245–253.
22 V. A. Barinov, V. A. Tsurin, V. I. Voronin, S. I. Novikov and V. T. Surikov, *Phys. Met. Metallogr.*, 2006, **101**(5), 456–466.
23 K. Momma and F. Izumi, *J. Appl. Crystallogr.*, 2008, **41**, 653–658.
24 A. Jain, S. P. Ong, G. Hautier, W. Chen, W. D. Richards, S. Dacek, S. Cholia, D. Gunter, D. Skinner, G. Ceder and K. A. Persson, *APL Mater.*, 2013, **1**, 011002.
25 M. Souissi, M. H. F. Sluiter, T. Matsunaga, M. Tabuchi, M. J. Mills and R. Sahara, *Sci. Rep.*, 2018, **8**(1), 1–9.
26 S. J. Pennycook and D. E. Jesson, *Ultramicroscopy*, 1991, **37**, 14–38.
27 J. Xie, N. Chen, L. Teng and S. Seetharaman, *Acta Mater.*, 2005, **53**, 5305–5312.
28 V. A. Barinov, V. A. Tsurin and V. T. Surikov, *Phys. Met. Metall.*, 2012, **113**, 48–61.
29 D. G. Quirinale, D. Messina, G. E. Rustan, A. Kreyssig, R. Prozorov and A. I. Goldman, *Phys. Rev. Appl.*, 2017, **8**(5), 054046.
30 C. M. Fang, M. A. van Huis, M. H. F. Sluiter and H. W. Zandbergen, *Acta Mater.*, 2010, **58**, 2968–2977.
31 A. R. Biedermann, *Geosciences*, 2018, **8**(8), 302.
32 F. Neumann and O. Meyer, *Vorlesungen über die Theorie der Elasticität der festen Körper und des Lichtäthers*, BG Teubner, 1885.
33 P. J. Dobson, *Phys. Bull.*, 1985, **36**, 506.